Influence of the electrolyte salt concentration on the rate capability of ultra-thick NCM 622 electrodes

Lea Kremer[a*], Timo Danner[b,c], Simon Hein[b,c], Alice Hoffmann[a], Benedikt Prifling[d], Volker Schmidt[d], Arnulf Latz[b,c,e], Margret Wohlfahrt-Mehrens[a]

[a] L, Kremer, Dr. A. Hoffmann, Dr. M Wohlfahrt-Mehrens
Akkumulatoren Materialforschung
ZSW - Zentrum für Sonnenenergie- und Wasserstoff-Forschung Baden Württemberg
Lise-Meitner-Straße 24, 89081 Ulm, Germany
E-mail: lea.kremer@zsw-bw.de
[b] Dr. T. Danner, Dr. S Hein, Prof. Dr. A. Latz
Institut für Technische Thermodynamik
DLR – Deutsches Zentrum für Luft- und Raumfahrt
Pfaffenwaldring 38-40, 70569 Stuttgart, Germany
[c] Dr. T. Danner, Dr. S Hein, Prof. Dr. A. Latz
HIU – Helmholtz-Institut Ulm
Helmholltzstraße 11, 89081 Ulm, Germany
[d] B. Prifling, Prof. Dr. V. Schmidt
Institut für Stochastik
Universität Ulm
Helmholtzstraße 18, 89081 Ulm, Germany
[e] Prof. Dr. A. Latz
Institut für Elektrochemie
Universität Ulm
Albert-Einstein-Allee 47, 89081 Ulm, Germany

Supporting information for this article is given via a link at the end of the document.

Abstract: In traditional Li-ion batteries, the electrolyte consists of a Li-conducting salt dissolved in organic solvents at a concentration of ~1 mol L^{-1} (1 M). In this work, we use increased $LiPF_6$ concentrations between 1 and 2.3 M to investigate the influence of the electrolyte salt concentration on the rate capability of ultra-thick (49.5 mg cm^{-2}) and thin (5.6 mg cm^{-2}) NCM 622 electrodes, respectively. At higher electrolyte salt concentrations than 1 M, thin electrodes suffer from increased polarization, due to a higher viscosity and a reduced ionic conductivity. In contrast, by raising the salt concentration from 1 to 1.9 M the discharge capacity of ultra-thick electrodes is increased by more than 50% for current densities above 3 mA cm^{-2}, which significantly improves their rate capability. 3D microstructure resolved simulations revealed that this effect results from the mitigation of Li-ion depletion in the electrolyte filled pore space of ultra-thick electrodes.

Introduction

Rechargeable Li-ion batteries (LIBs) enabled the wireless revolution of all kinds of mobile electronic devices, e.g. cell phones or laptop computers. Furthermore, LIBs started to supersede the internal combustion engine by powering electric vehicles[1] and thus have transformed transportation and global communication since their first commercialization by Sony in 1991[2].

A battery is composed of one or more interconnected electrochemical cells, in which each cell consists of two electrodes, the anode and the cathode, separated by a separator soaked with electrolyte.[3] The electrolyte in a Li-ion battery cell serves as an electrically-insulating medium enabling efficient ionic transport between the two electrodes to maintain charge balance. Simultaneously, it must withstand the strong reducing and oxidizing forces of the negative and positive electrode, respectively[4,5]. Traditionally used electrolytes are composed of a Li-salt, most commonly used is $LiPF_6$, dissolved in an organic solvent mixture of ethylene carbonate (EC) and low-viscosity linear carbonate, e.g., dimethyl carbonate (DMC), diethyl carbonate (DEC), and ethyl methyl carbonate (EMC). Moreover, conventional electrolytes contain diverse additives, e.g. vinylene carbonate (VC) for the formation of a stable SEI. Therein the electrolyte salt concentration is typically around 1 mol L^{-1} (hereafter referred to with the term “1 M electrolyte”), where the ionic conductivity reaches the maximum value and a trade-off between a large number of dissociated ions and a moderate viscosity is attained. This basic electrolyte composition has remained almost unchanged for over two decades, ever since the first commercialization of Li-ion batteries.

Despite their decreased ionic conductivity and increased viscosity, highly concentrated electrolytes recently received attention of several research groups, since they offer unique properties compared to electrolyte with commonly used salt concentrations (~1 M). Highly concentrated electrolytes show intriguing features, which are often related to the change of the Li-Ion solvation structure and the drastically decreasing number of free non-solvating solvent molecules in the literature. These features include an increased oxidative and reductive stability, fast and reversible Li-ion insertion/extraction as well as the suppression of Li-metal dendrite formation and inhibition of Aluminum corrosion[5–7]. Furthermore it has been demonstrated that by using elevated electrolyte salt concentrations, Li-ion depletion in the electrolyte phase can be mitigated, which occurs if thick electrodes are operated at high current densities[8,9]. This Li-ion depletion usually results in a low rate capability, which is one main drawback that hinders the widespread application of ultra-thick electrodes, despite their numerous benefits compared to electrodes with thicknesses according to the state of the art.

Increasing the electrode thickness generally gives access to higher areal capacities, which enables lowering the absolute number of layers in the cell stack resulting in a better active to passive material ratio. This saves passive materials such as current collectors and separators, which reduces the cell price and simultaneously makes the battery more sustainable. Therefore, these ultra-thick electrodes allow a higher energy density at lower battery costs compared to state of the art LIBs, which are both key features for a widespread commercialization of future electric mobility. Du et al investigated different strategies to overcome the transport limitations of thick electrodes and performed numerical simulations to show, that the increase in initial electrolyte molarity raises the whole concentration gradient profile. This effect resulted in reduced electrolyte depletion in an NCA electrode with a thickness of 180 µm[8].

However, in their simulations the authors neglected the concentration dependence of transport parameters, which we implemented in our model. Moreover, our studies show the importance of electrode microstructure, as well as carbon black and binder morphology[10], on the ionic transport, especially in thick electrodes[11,12].

To the best of our knowledge, there is no experimental study reported in the literature that systematically investigates the relationship between the electrolyte salt concentration and the rate capability of electrodes with different thicknesses. For this reason, we prepared two $LiNi_{0.6}Co_{0.2}Mn_{0.2}O_2$ (NCM 622) positive electrodes with extremely different mass loadings and cycled both of them in half-cells using electrolytes with five different elevated $LiPF_6$ concentrations. Subsequently, the rate capability, energy and power density of both electrodes at all $LiPF_6$ concentrations was compared to derive the specific impact of the electrolyte salt concentration on high-power and high-energy Li-ion battery cathodes.

The systematic experiments are supported by microstructure resolved simulations, which provide additional insights on salt concentrations within the cell, as well as predictions on the effect of different salt concentrations on full cell performance. Our study closes a gap in the research on ultra-thick electrodes and indicates the potential of this approach.

Results and Discussion

Slowing down the charging and discharging rates has been the greatest concern about the use of highly concentrated electrolytes, which has excluded them from the mainstream of research and development in Li-ion batteries until quite recently. This concern may arise from the basis of the aforementioned decrease in ionic conductivity and increase in viscosity at higher concentrations than 1 M, which indeed result in poor rate performance with highly concentrated electrolytes in most cases. However, exceptions to these restrictions do exist[5]. In order to compare the influence of the electrolyte salt concentration on the rate capability of thin and ultra-thick electrodes, two NCM 622 cathodes with extremely different mass loadings were prepared from the same suspension under equal conditions, using the same proportion of active material (AM), carbon black (CB), graphite (G) and binder (B) in a ratio of 93:2:1:4. In Table 1 the physical and electrochemical properties of the two NCM 622 positive electrodes are summarized. The very thin electrode with an areal capacity below 1 mAh cm^{-2} can be referred to as a high-power electrode, since it is capable to operate at high current densities, whereas the ultra-thick electrode with more than 8 mAh cm^{-2} can be referred to as an ultra-high energy electrode, which is more applicable at lower current densities.

Table 1. Physical and electrochemical properties of NCM 622 cathodes with two different mass loadings and a similar composition of AM, CB, G and B in a ratio of 93:2:1:4.

Electrode description	Total mass loading (mg cm^{-2})	AM mass loading (mg cm^{-2})	Areal capacity @ C/10 (mAh cm^{-2})	Electrode composite thickness (µm)	Electrode composite density (g cm^{-3})
Thin electrode (high-power)	5.6	5.2	0.95	22	2.6
Ultra-thick electrode (high-energy)	49.5	46.0	8.10	161	3.0

Figure 1 displays the electrochemical performance of the thin (dotted lines and round symbols) and the ultra-thick (solid lines and square symbols) NCM 622 positive electrodes in half-cell configuration with a 1 M electrolyte solution. On the left side, the dependence of the capacity retention relative to the respective accessible discharge capacity Q at 1 mA cm^{-2} is shown as a function of the current density. From this figure, it becomes obvious that expectedly, the thin electrode has a higher rate capability than the ultra-thick electrode, which shows a pronounced capacity drop on higher current densities than 3 mA cm^{-2}. On the right side of Figure 1, the voltage curves of both cells plotted against their respective AM-specific capacities at three different discharge current densities (1, 6 and 10 mA cm^{-2}) are presented.

At 1 mA cm^{-2} both electrodes follow a similar course until the thin electrode suddenly drops to the discharge cut-off voltage (3.0 V) at a lower capacity than the ultra-thick electrode, which is related to the about eight times higher C-rate that the thin electrode perceives compared to the thick one. At higher current densities, the thin electrode shows a stronger IR-drop, due to its smaller active surface, but a higher active material utilization, whereas the ultra-thick electrode has a less pronounced IR-drop, but delivers only 20% of its initial discharge capacity at 10 mA cm^{-2} which corresponds to 1.25 C.

Zheng et al.[13], Yu et al.[14], Danner et al.[12] and Gallagher et al.[15] demonstrated that transport within the electrolyte is the primary limitation for discharging thick electrodes, due to concentration gradients . that form between the electrodes and lead to non-uniform current distributions and underutilization of the AM.

During the operation of an electrochemical cell, mass must be transported from one electrode to the other through the electrolyte to bring reactants to the interfaces. The mass transport processes in an electrolytic solution mainly comprises three contributions, which allow to describe the motion of mobile ionic species. These processes are i) migration, caused by the applied electric field; ii) diffusion, caused by concentration gradients and iii) convection, due to the movement of bulk electrolyte solution[16]

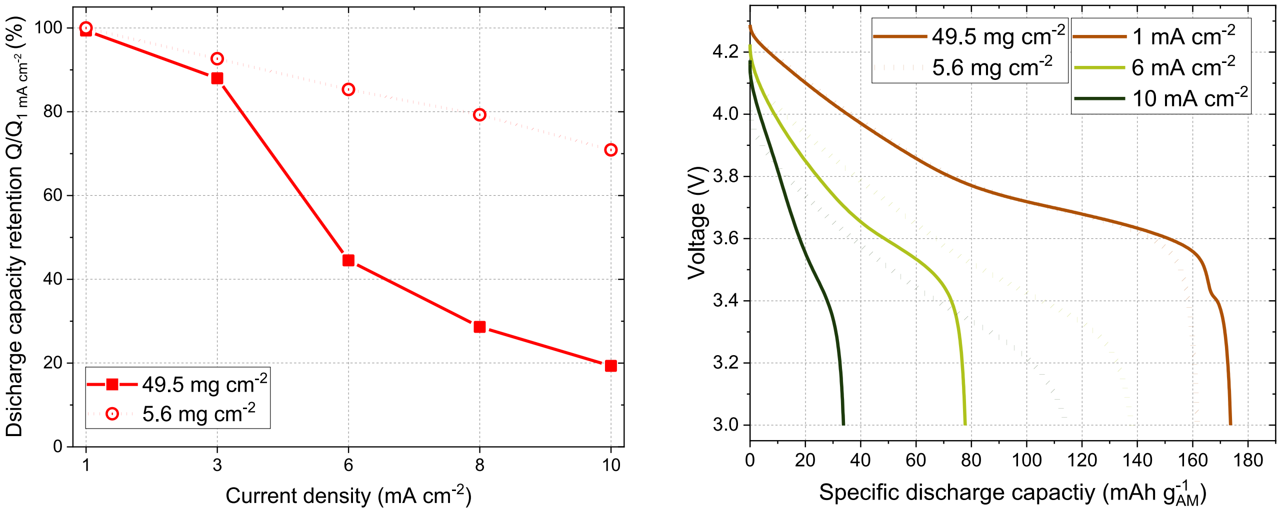

Figure 1. Electrochemical measurements of the thin (dotted lines) and the ultra-thick (solid lines) NCM 622 positive electrodes in half-cells with a 1 M electrolyte. Left: Discharge capacity retention with respect to the discharge capacity of the corresponding electrode at 1 mA cm^{-2} and right: Voltage curves as a function of the respective active material-specific capacities at discharge current densities of 1, 6 and 10 mA cm^{-2}.

However, the contribution of the latter one is often negligible, since convective transport is highly unlikely under normal operating conditions in a battery[17]. In general, the mass transport of Li-ions can be described by three characteristic macroscopic values: 1) the electrolytic conductivity κ, that is related to the total flux of charge carriers, 2) the Li$^+$ diffusion coefficient D_{Li^+} and 3) the Li-ion transference number t_{Li^+}, which is related to the fraction of the total current I carried by Li-ions[18].

$$t_{Li^+} = \frac{I_{Li}}{\sum_i I_i}$$

At typical electrolyte concentrations, transference numbers of Li-ions usually range between 0.2 and 0.4, dependent on salt and solvent properties. Since Li-ions are small, hard cations and bear a high surface charge density, they are favorably solvated and must therefore move at slower speed with their solvation sheath than the anions. Results obtained from various modelling approaches including ab initio quantum mechanics showed that Li$^+$ is usually solvated by a maximum of four molecules in a tetrahedral environment, due to its small ionic radius[19–22].

In contrast, large and soft anions like PF_6^- are less polarizable and therefore high populations of anions remain relatively unsolvated and much more mobile than the solvated Li-ions[23]. Additionally, in most cases, polar aprotic solvents like EC or EMC work as Lewis bases and tend to coordinate to cations (Lewis acids) rather than to anions (Lewis base) [5].

Since only one part of the current goes into the transference of Li-ions, Li$^+$ is consumed at the interface to the positive electrode and/or released at the negative faster than it is replenished by electrical migration. Due to this time lag, a gradient in salt concentration of the electrolyte builds up between both electrodes in the cell. The formation of this concentration gradient then drives the diffusion of the salt, which constitutes for the rest of the transport of Li$^+$ that is not supplied by migration and can ultimately limit the discharge (or charge) of the battery. If the concentration of salt at an electrode surface reaches zero, the ionic resistance becomes extremely high, which results in a sudden jump or drop to the cut-off voltage terminating the charge or discharge process. In contrast, if the concentration of salt becomes too high and the solubility limit is exceeded, the salt can precipitate and again, the resistance can get extremely high. However, both processes are reversible in time. The extent and velocity of the concentration gradient formation is not only dependent on the applied current density, but also on the values of t_{Li^+} and D_{Li^+}[24]. Both parameters significantly change when the electrolyte salt concentration is varied (see SI).

Figure 2 shows the current density dependence of the AM-specific discharge capacitiy (left) and the relative discharge capacity compared to the specific capacity using a 1 M electrolyte (right) of half-cells with the thin and the ultra-thick NCM 622 electrodes with five different $LiPF_6$ concentrations. These results indicate a clear difference in the influence of the electrolyte salt concentration on the rate capability of the ultra-thick and the thin electrode, respectively. The thin electrode retains mostly constant discharge capacities throughout all concentrations, while the discharge capacity of the ultra-thick electrode increases steadily with increasing concentration of conductive salt compared to the 1 M concentration (red symbols), until it reaches the highest value at a concentration of 1.9 M (green symbols). At this optimal concentration, the discharge capacity of the ultra-thick electrode is increased by more than 50% at all current densities between 6 and 10 mA cm^{-2}. However, when the optimal concentration is exceeded as shown for the concentrations 2.1 M (turquoise symbols) and 2.3 M (blue symbols), the respective discharge capacities at all current densities decline again.

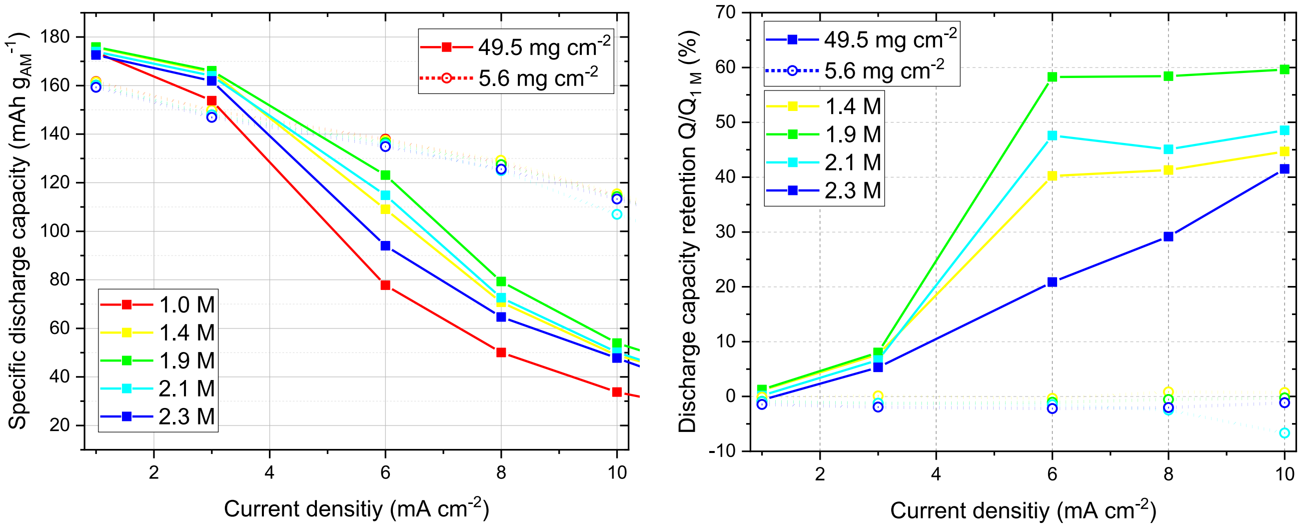

Figure 2. Rate capability test at current densities between 1 and 10 mA cm^{-2} of a thin (dotted line and round symbols) and an ultra-thick (solid line and square symbols) NCM 622 cathode with the same composition, built in half-cells using electrolytes with five different $LiPF_6$ concentrations in EC:EMC (3:7) +2% VC. Left: specific discharge capacity and right: relative discharge capacity compared to specific capacity at the same current density using a 1 M electrolyte.

In this study, we perform simulations on the continuum scale in order to monitor concentration distributions within the cell during operation. Details of the simulation approach as well as simulated discharge curves of the corresponding half-cell experiments can be found in the Supporting Information. Figure 3 presents snapshots of the electrolyte concentration within the pore-space of the ultra-thick cathode after around 2100 s during a discharge with 6 mA cm^{-2}. At the initial salt concentration of 1 M we observe complete salt depletion of the electrolyte solution close to the current collector. Only close to the separator significant Li-ion concentration is predicted which limits the utilization of the active material. At higher salt concentrations, the overall concentration level in the electrode increases and a significantly larger part of the electrodes contributes to the capacity. The active electrode volume with on-vanishing electrolyte concentration indicated by green to red color is similar in simulations with 1.9 M and 2.1 M initial concentration. However, at an initial salt concentration of 2.1M, the local salt concentration close to the separator already reaches up to 3 M. The simulations indicate that in this case concentrations close to the anode surface even exceed the solubility limit. As discussed above high concentrations cause larger ohmic losses, which eventually will reduce cell capacity. In order to interpret these findings in further detail, the change of the electrolytic composition and structure with increasing salt concentration is inspected in the following section.

Figure 3: Concentration of Li-ions in the electrolyte within the pore space of the ultra-thick NCM 622 cathode during lithiation simulations at 6 mA cm^{-2}. The initial salt concentration increases from left to right (c_0 = 1.0, 1.9, 2.1 M).

Jow and co-workers claimed that the dependence of the electrolytic conductivity κ on the molar salt concentration M can satisfactorily be be explained by the following three factors i); The number of dissociated ions per unit volume of the electrolyte solution ii) the dielectric constant of the solvent ε and iii) the viscosity of the electrolyte η[25].

Figure 4 shows the measured concentration dependence of the electrolytic conductivity κ, kinematic viscosity ν and dynamic viscosity η at 25 °C for our EC/EMC based electrolyte and $LiPF_6$ concentrations between 1 and 2.3 M. The kinematic and dynamic viscosity are related via the density ρ by the following expression:

$$\eta = \nu \cdot \rho$$

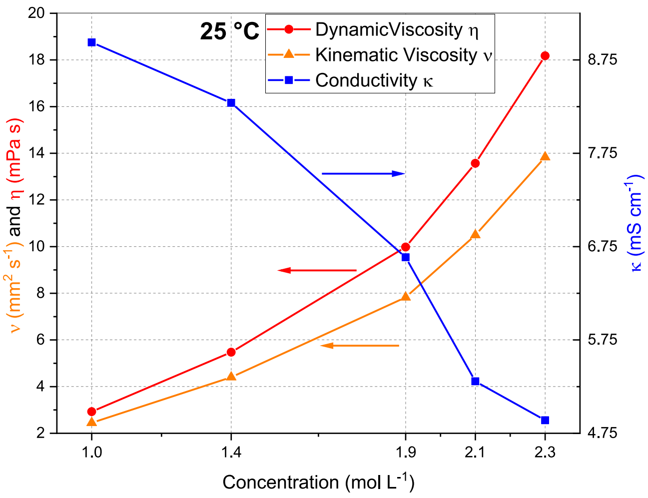

Figure 4. Change of kinematic (orange) and dynamic (red) viscosities and ionic conductivities (blue) of all five electrolytes at 25 °C with increasing $LiPF_6$ concentration.

Concentration dependences of κ, ν and ρ at temperatures between 10 °C and 80 °C are shown in Figure S 1 in the Supporting Information.

It is generally accepted, that in diluted electrolyte systems below concentrations of 1 M, the conductivity increases with increasing salt concentration, due to the increased number of dissociated solvent-separated ion pairs in the electrolyte solutions. With further increase of the salt concentration above 1 M, the cationic and anionic species form contact ion pairs (CIPs) and agglomerates (AGGs) which do not contribute to conductivity since only dissociated, unpaired ions that carry a net charge can migrate in the electric field[5,18].

Due to the simultaneous increase in viscosity η (see Figure 4), the overall electrolytic conductivity, ionic mobility and the diffusion constants of all species decrease with increased salt concentration. However, the decrease in the diffusion constant is more pronounced for the anions (here: PF_6^-) than for Li^+. The reason for this disparate concentration dependence is the dissimilar change in the volume of the resulting complexes for anion and cation. Upon the formation of an ion pair, the cation only exchanges a solvent molecule against the anion or adds the anion in the solvation sphere, which does not considerably change the Li^+ diffusion coefficient. In contrast, the incorporation of the anion into an ion pair leads to a large volume increase of the resulting complex and therefore a large decrease of the diffusion coefficient of the anion. Thus, the stronger concentration dependence of the anion diffusion coefficient compared to the diffusion coefficient of the lithium cation can be tentatively explained by different solvation energies[26].

Self et al.[27] investigated the transport in $LiPF_6$/Propylene Carbonate (PC) Electrolytes at concentrations ranging from 1 to 3 M and reported that due to the difference in the concentration dependence of the cationic and anionic diffusion constants, the ratio of

$$\frac{D_{Li^+}}{D_{Li^+} + D_{PF_6^-}}$$

, which is sometimes referred to as the lithium ion transport number, increases with increasing salt concentration between 1 and 3 M.

In the electrolytes used for our study, the conductive salt and the concentration range were similar to [27], but instead of PC the solvent is composed of a mixture of EC and EMC in the weight ratio 3:7.

In this solvent mixture, the Li-ion is preferentially solvated by EC, rather than by EMC, due to its higher dielectric constant ε (At 25 °C: $\varepsilon_{EC} = 89.78 >> \varepsilon_{EMC} = 2.958$[23]) and solvation power. Table 2 summarizes the composition and properties of all electrolytes used in this study as well as the average ratios of both solvent molecules in proportion to the respective amount of $LiPF_6$.

Table 2. Properties of five different electrolytes with $LiPF_6$ salt concentrations ranging between 1.0 and 2.3 M.

c($LiPF_6$) (mol L^{-1})	Molality (mol kg^{-1})	Density at 25 °C (g cm^{-3})	mol(EC)/ mol($LiPF_6$)	mol(EC+EMC)/ mol($LiPF_6$)
1.0	0.8	1.19	3.6	10.6
1.4	1.2	1.24	2.4	7.0
1.9	1.5	1.28	1.8	5.2
2.1	1.6	1.29	1.6	4.6
2.3	1.7	1.31	1.4	4.2

In general, a solvent with a high dielectric constant shields the ions of one charge from the attraction of those of the opposite charge, thus preventing ion association in the electrolyte[25]. At a concentration of 1 M there are 3.6 molecules of EC available for each Li-ion, which allows for a first solvation sheath that is exclusively composed of EC. When the $LiPF_6$ concentration increases, the EC:$LiPF_6$ ratio decreases steadily to 1.4 at the highest concentration that was used in this work. This decrease of free EC molecules indicates that the structure and size of the Li^+ solvation sheath changes upon increasing salt concentration, because an increasing amount of the larger EMC molecules needs to be incorporated into the Li^+ solvation sheath. Since a higher number of EMC in the solvation sheath is associated with a larger size of the resulting complex, it can be assumed that the accordingly larger EMC-solvated Li-ion complexes travel slower in an electric field than the smaller EC-solvated Li-ion complexes. However, to achieve better ionic transport properties for fast discharging of ultra-thick electrodes, both must be maximized, the mobility of dissociated Li-ions, as well as the charge carrier density, which influences the kinetics of the intercalation reaction by the increase of the pore to wall flux [6,8]. Therefore, we conclude that for the ultra-thick electrode used in this study, the trade-off between the beneficial effect of a high initial charge carrier density and the slower diffusion, due to an increased amount of CIPs and AGGs results in an optimum electrolyte salt concentration of around 1.9 M.

These changes in the electrolyte composition with increasing concentration also affect the galvanostatic charge and discharge profiles of the half-cells of the thin (left) and the ultra-thick (right) electrodes shown in Figure 5. The voltage curves during charge and discharge were recorded at a constant current (CC) of 1 mA cm^{-2}. Subsequently to the CC charging step, a constant voltage (CV) step at 4.3 V was conducted to achieve complete delithiation of the NCM electrodes. From these voltage profiles, it becomes obvious that upon increasing the salt concentration, the average voltage increases during charging and decreases during discharge. This applies to both electrode thicknesses and is related to a higher polarization, which occurs already at the lowest current density of the rate capability test.

Polarization refers to a lack or excess of electrode potential compared to equilibrium, due to side-effects at the interface between electrode and electrolyte. Therefore, the actual electrode potential E is always larger (during charging) or smaller (during discharging) than the equilibrium potential E_{eq}[28]. Since each battery component undergoes charge-transfer at different rates, the slowest transfer becomes the rate-limiting process.

The cell polarization can be classified into ohmic polarization (IR-drop), activation polarization, and concentration polarization and is equivalent to the applied current multiplied by the internal resistance of the cell. The internal cell resistance includes contributions of the electronic resistance in the solid phase (AM and carbon binder domain), the ionic resistance in the electrolyte phase, the Li-ion charge-transfer resistance at the electrode/electrolyte interface and Li-ion diffusion impedance in the solid phase[8]. The electrolytes used in commercial LIBs usually exhibit large concentration polarization due to comparatively low Li^+ transference numbers and salt diffusivities, and thus the polarization is largely related to the transport properties[29]. Even though these different types of polarization are difficult to distinguish in an actual battery[28], simulation based approaches like the one presented in this study are able to discriminate the different contributions and provide indications on limiting processes.

In both graphs of Figure 5, the IR drop increases with increasing electrolyte salt concentration, which indicates a strong contribution of the electrolyte resistance to the overall cell polarization. One characteristic parameter for the cell polarization during discharge is the decline of the average discharge voltage $V_{average}$ obtained from the cell voltage curve at a certain current density[8]:

$$V_{\text{average}} = \frac{\int_0^Q V(q)dq}{Q}$$

As presented Figure 6, the average discharge voltages of both electrodes decrease with increasing current densities between 1 and 10 mA cm^{-2} since the IR-drop and overvoltage from polarization increase with discharge current[28]. At higher concentrations than 1 M, ohmic polarization will be the major contributor to overall polarization originating from the electrolyte, since the ionic conductivity is comparatively low[30].

Apparently, the decrease of $V_{average}$ upon the increase in the electrolyte salt concentration is more severe for the ultra-thick electrode than for the thin electrode. One possible explanation for this observation is that thicker electrodes suffer from higher internal resistance growth at a similar current density than thin electrodes, since the absolute path length for electronic and ionic conduction increases.

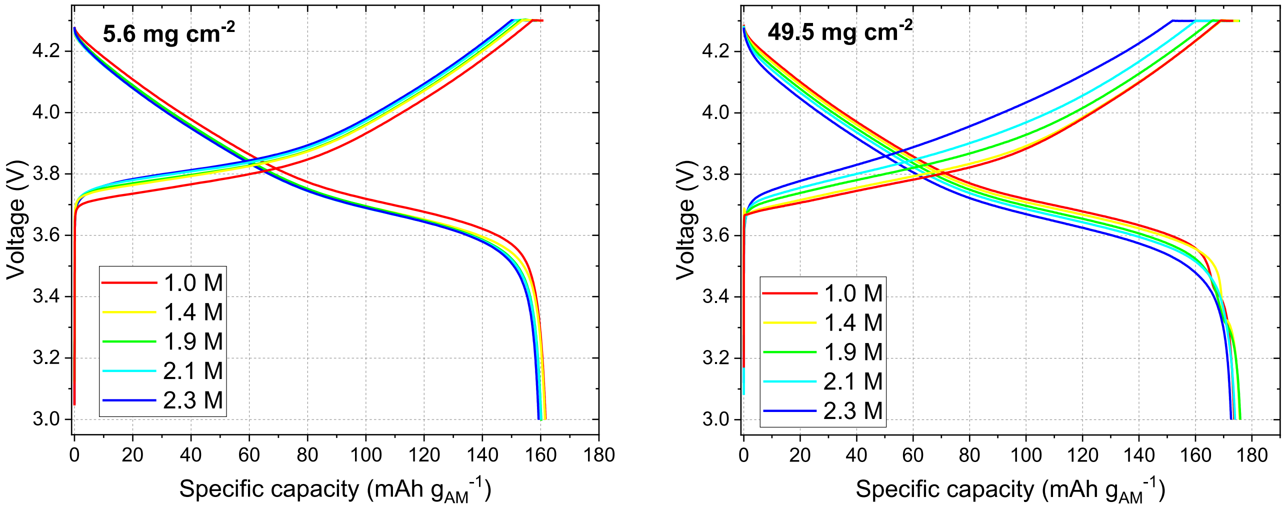

Figure 5. Voltage curves of the thin (left) and the ultra-thick (right) NCM 622 cathodes in half-cells at five different $LiPF_6$ salt concentrations in the EC/EMC based electrolyte at 1 mA cm^{-2}.

From the comparison of the voltage curves in Figure 5, it also becomes obvious that for the ultra-thick electrode, the increase in polarization during charging is more pronounced than during discharging. This is a direct consequence from the inversion of the Li^+ gradient upon changing the direction of the current flow, which results in Li^+ enrichment at the positive electrode and Li^+ depletion at the negative electrode.

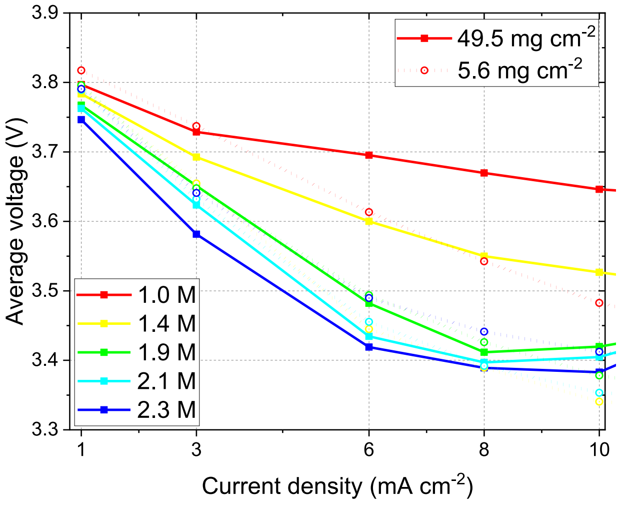

Figure 6. Average discharge voltages of the thin (dotted line and open symbols) and the ultra-thick (solid line and filled symbols) NCM 622 electrodes.

As previously discussed, the Li^+ migration from positive to negative electrode is increasingly hindered when along with the salt concentration, the electrolyte viscosity grows. Contrary to the NCM electrodes, the Li-metal is non-porous and exhibits a comparatively small surface area; therefore, the small electrode/electrolyte interface limits the charge transfer reaction during charge in contrast to the discharge process. Furthermore, the duration of the potentiostatic charging step as well as the CV/CC capacity ratio both grow with increasing thickness and salt concentration, as can be seen in Figure 5.

These findings also indicate that the higher density of charge carriers in the electrolyte, that has a beneficial impact on ultra-thick electrodes during discharging, impedes the charging process when the concentration gradient is reversed.

However, these adverse consequences resulting from increased salt concentrations could be addressed by reducing the resistance associated with electrolyte. For a specific application in cells with ultra-thick electrodes, we propose a tailored electrolyte composition. There are numerous strategies published in the literature to improve electrolyte properties, such as conductivity and Li-ion mobility. In order to increase the Li^+ transference number and the degree of dissociation, Li-salts with well-stabilized anions with a large radius and electron-withdrawing functionalities such as bis(fluorosulfonyl)imide FSI^-[18,31] and solvents with high dielectric constants are desirable. To achieve a higher ionic mobility and a higher Li^+ diffusion coefficient, the viscosity of concentrated electrolytes must be lowered, which was successfully demonstrated through the adjustment of the EC solvent ratio[25] as well as by dilution with a low-polarity solvent[6]. Furthermore, the addition of co-solvent such as Methyl acetate (MA)[32] as well as the adoption of higher operating temperature might be beneficial, since an increase in temperature favors dissociation and mobility of the ions due to the additional thermal agitation[25].

The electrode energy U takes into account both, the AM utilization denoted by the capacity Q as well as the polarization represented by the average voltage $V_{average}$:

$$U = Q \cdot V_{average}$$

In order to investigate the extent to which the beneficial effect of increased electrolyte salt concentrations on the discharge capacity of ultra-thick electrodes compensates the higher polarization, specific energy and energy density of both electrodes were calculated and displayed in Figure 7.

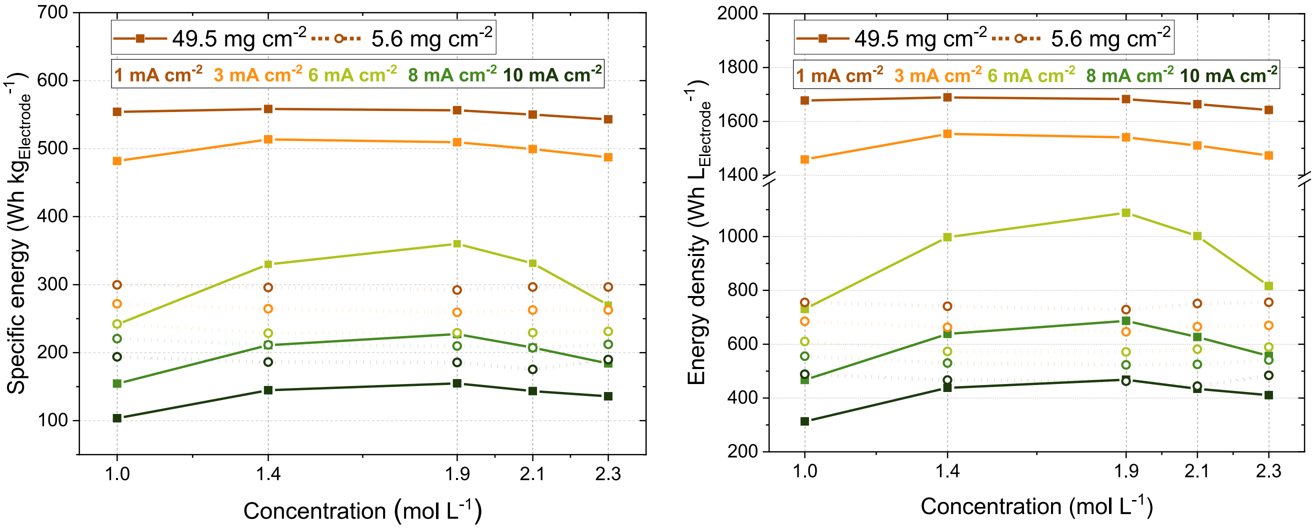

Figure 7. Specific energy (left) and energy density (right) calculated on the electrode level incl. the Al current collector for the thin (dotted line and round symbols) and the ultra-thick (solid line and square symbols) NCM 622 electrodes for five different current densities and electroyte concentrations.

At low current densities, the specific energy and energy density generally increase with the increase of the electrode thickness[8], due to an increased ratio of active and passive materials. This beneficial effect of the electrode thickness is even more pronounced in case of the electrode energy density (see Figure 7 right) compared to the electrode specific energy (see Figure 7 left). The reason for this difference is that the Al current collector adds a relative high portion to the total electrode volume compared to the active material but only a comparatively small mass fraction.

Furthermore, the diagrams in Figure 7 prove, that by using concentrated electrolytes, the specific energy and energy density of ultra-thick electrodes can both be significantly increased and largely exceed the respective energy of a thin electrode, even at rather high current densities of 6 mA cm^{-2} and more. Even though the higher electrolyte concentrations are associated with higher costs, since the conducting salt in the electrolyte is generally more expensive than the solvents, this strong benefit legitimizes the use of concentrated electrolytes from the author's perspective. With a conductive salt concentration of 1.9 M, the measured energy density and specific energy on the electrode level both show a maximum at all current densities above 3 mA cm^{-2}. At lower current densities of 1 and 3 mA cm^{-2}, the optimal concentration is shifted to slightly lower concentrations, although the differences between the individual energies at all concentrations are rather small.

The focus of our investigation lies on the performance of ultra-thick NMC 622 cathodes at elevated electrolyte salt concentrations. Therefore, we use a half-cell configuration in our experiments in order to eliminate mass transport affects associated with the anode microstructure. However, evaluation of the effect of increased salt concentrations in full battery cells consisting of ultra-thick cathodes and anodes is important for future research directions. While the fabrication of such cells is challenging, due to the mechanical properties of ultra-thick anode films, simulations allow to assess expected trends. Therefore, we performed full cell simulations using the cathodes presented in this work and matching graphite anodes with a theoretical areal capacity of 9 mAh cm^{-2}. The corresponding simulation results are presented in Figure 8.

Similar to our half-cells measurements (cf. solid circles in Figure 8) we predict an increase in energy density also in full cell configuration at currents beyond 6 mA cm^{-2}. Depending on the effective transport properties in the electrolyte, which result from the electrode microstructure and the CBD morphology (see SI for more Information), we expect an increase in energy density of up to 50% at electrolyte salt concentrations of 1.8-1.9 M compared to the respective value of full cells with an electrolyte salt concentration of 1 M. It is worth noting that with decreasing effective transport properties a larger relative increase can be expected. However, absolute energy densities are of course lower in this case. The corresponding simulated discharge curves are presented in Figure S 8.

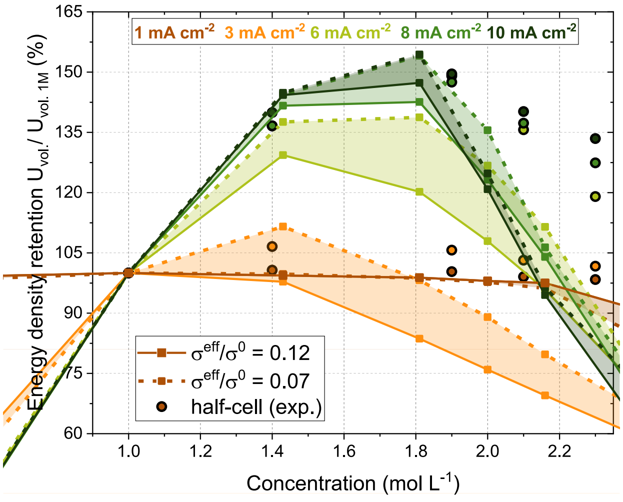

Figure 8. Energy density obtained by full cell simulations. Values are relative to energy density at the same current using a 1 M electrolyte. Dashed and solid lines indicate simulation results with two different effective conductivities and shaded areas indicate corresponding expectation values. Experimental data of half-cell measurements represented by solid circles is included as reference.

Figure 9 summarizes in a Ragone plot the power and energy densities of the thin (round symbols) and the ultra-thick (square symbols) electrodes at all current densities and electrolyte salt concentrations. Magnifications of individual regions in the Ragone plot for both electrodes are available in Figure S 2 of the Supporting Information.

As expected and previously discussed, the thin electrode is largely independent on the electrolyte salt concentration and most suited for high-power applications, where high currents need to be tolerated. In contrast, at a rather low current density of 1 mA cm^{-2}, the ultra-thick electrode offers very high energy densities of more than 1600 Wh L^{-1} on the electrode level, which is more than twice the energy density of the thin electrode at the same current density.

Even though the operation of thick electrodes is only reasonable until a critical current density is reached, which in this case corresponds to 6-8 mA cm^{-2}, this critical current density can be shifted to higher values if the electrolyte salt concentration is optimized as demonstrated in this work.

Remarkably, at an electrolyte salt concentration of 1.9 M and an equal C-Rate of 1 C (1 C roughly corresponds to 1 mA cm^{-2} for the thin and 8 mA cm^{-2} for the ultra-thick electrode), the power density of the ultra-thick electrode exceeds the power density of the thin electrode by 75%, while its energy density maintains a comparable level (6% less than the thin electrode). Moreover, at an intermediate current density of 6 mA cm^{-2} (≈ 0.75 C for the ultra-thick electrode and 6 C for the thin electrode), the ultra-thick electrode with a concentrated electrolyte can still deliver a higher energy and power density than a thin electrode at 1 mA cm^{-2} (≈ 1 C).

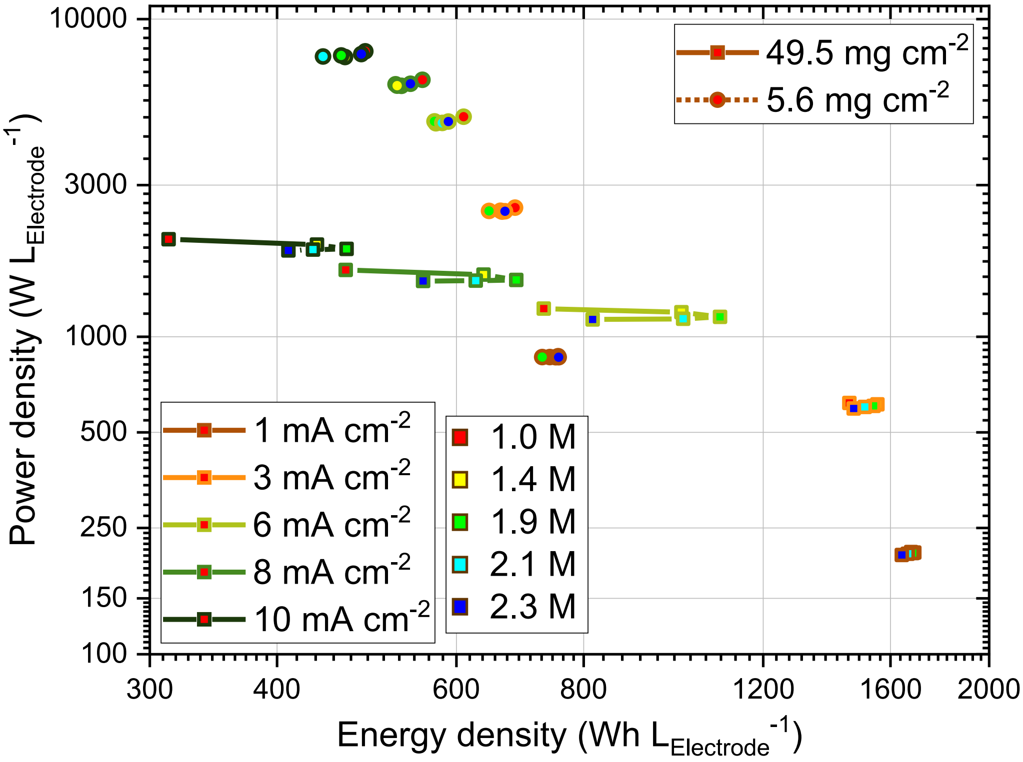

Figure 9. Ragone plot of thin (dotted line and round symbols) and ultra-thick (solid line and square symbols) NCM 622 cathodes calculated on the electrode level incl. the current collector for five different discharge current densities and electrolyte concentrations.

Conclusion

Positive electrodes in Li-ion batteries are usually customized for their respective application. For power devices, electrodes are necessarily thin to withstand high current densities. For energy applications, thick electrodes offer a desirable active to passive material ratio, achieving lower costs and higher sustainability than state of the art or thin electrodes. However, their rate capability is limited by the Li-ion mass transport in liquid electrolytes, due to the formation of concentration gradients. For electrode thicknesses according to the state of the art, it is generally acknowledged that ~1 M is the conventionally used concentration for conductive salts in Li-ion battery electrolytes to achieve a trade-off among ionic conductivity, viscosity, and cost[33].

In this work, the influence of higher LiPF$_6$ salt concentrations between 1 and 2.3 M in an EC/EMC based electrolyte was investigated with regard to the use in Li-ion cells with thin high-power and ultra-thick high-energy electrodes. In order to examine these borderline cases, two NCM 622 electrodes with extremely different mass loadings (5.6 and 49.5 mg cm^{-2}) were prepared and their electrochemical performance at five different electrolyte salt concentrations was systematically evaluated.

For the ultra-thick electrode, it was demonstrated that concentrated electrolytes allow significantly larger discharge capacities at current densities above 3 mA cm^{-2} compared to commonly used electrolytes. This is most pronounced at a $LiPF_6$ concentration of 1.9 M, where the respective capacities compared to the cells with a salt concentration of 1 M was increased by more than 50% at all current densities between 6 and 10 mA cm^{-2}. In contrast to this observation, the discharge capacity and rate capability of a thin electrode showed no remarkable concentration dependency.

Increasing the $LiPF_6$ concentration by simple salt addition does not require any significant change or additional investment to the present manufacturing facility[5] but results in a mitigation of the Li-ion depletion, which occurs in the electrolyte filled pores close to the current collector when ultra-thick electrodes are operated at higher current densities. Microstructure resolved simulations confirm that the additional Li-salt in the electrolyte introduces an elevated charge carrier density and thus allows activating larger parts of the thick electrode resulting in higher discharge capacities before transport limitations take over.

However, the increase in the salt concentration leads to a lower ionic conductivity and a higher electrolyte viscosity, which results in additional cell polarization. This stronger polarization leads to an overvoltage for concentrated electrolytes, which was observed especially during charging of the half-cell when the concentration gradient is reversed. Furthermore, our simulations indicate that locally concentrations are close to or even above the solubility limit of the electrolyte solution. This aspect certainly deserves more attention, both in model development and cell optimization.

Nevertheless, our experimental results in half-cells demonstrated that the combination of increased electrolyte salt concentrations and ultra-thick electrodes can deliver extremely high electrode specific energies and energy densities that largely exceed the respective energy of a thin electrode, even at rather high current densities of more than 6 mA cm^{-2}. Moreover, our simulations predict that a similar increase in energy density can also be attained in full cells with ultra-thick electrodes. Above all, the straightforward strategy of using increased electrolyte salt concentrations was demonstrated to enable an increase of the critical current density for high-energy electrodes that determines their rate-capability and therefore allows expanding the reasonable scope of application for ultra-thick electrodes significantly.

Experimental Section

Electrodes preparation.— The composite positive electrodes were prepared using the active material $LiNi_{0.6}Co_{0.2}Mn_{0.2}O_2$ (NCM 622, BASF), conductive additives and polyvinylidene fluoride binder (PVDF, Solvay Solexis) in the weight ratio 93:3:4. N-methylpyrrolidone (NMP, Sigma Aldrich) was used as solvent. All materials and substrates were used as delivered. A solution of the PVDF binder in NMP was freshly prepared with a total solid content of 7%. To this solution, the carbon black powder was added in one portion under stirring for 1 h at a maximum circumferential speed of 500 rpm, followed by the addition of graphite under the same conditions, increasing the total solid content to 12%. The active material was added in three portions at 200-500 rpm over a period of 1.5 h and subsequent stirring for 30 min until the final total solid content (TSC) of 63.55% was reached. The suspension was left overnight under reduced pressure and agitated next day, immediately before coating thin and ultra-thick films. The current collector substrate was an aluminum foil (Korff AG, Switzerland) with a thickness of 20 µm. The electrodes were coated and dried using an electrode coating pilot line (LACOM GmbH, Germany) with a comma bar system and four different drying zones (total length: 8 m). The speed of the coating was set to 1.5 m min^{-1}. After coating, the ultra-thick electrode composite was calendared to a density of 3.0 g cm^{-3} whereas the thin electrode composite was less compressible, which is the reason for its lower density of 2.6 g cm^{-3}.

Cell preparation and electrochemical characterization.—The electrodes were punched into discs of 1.2 cm diameter (area of 1.131 cm^2) and thoroughly dried for 16 h at 130 °C under vacuum. Half-cells were assembled by using 2032 coin cells in which lithium foil was used as a counter electrode. Two layers of a GF/A (Whatman glass fiber) were employed as a separator. The basic electrolyte used was 1.0 M $LiPF_6$ in a mixture of ethylene carbonate and ethyl methyl carbonate (ratio 3:7 by weight) with an additional 2 wt.% of vinylene carbonate (UBE), to which further $LiPF_6$ (Sigma-Aldrich, battery grade) was added to obtain the five different concentrations summed up in Table 2. Galvaostatic tests were carried out using a cell test system from BaSyTech GmbH (Germany). After assembling, the cells were allowed to rest for 24 hours, before they were conditioned by three consecutive, galvanostatic cycles at C/10 between 3 and 4.3 V with a consecutive constant voltage step at 4.3 V. Thereafter, a rate capability test was started to examine the capacity utilized as a function of discharge rate. The rate capability test involved three consecutive cycles at 1 mA cm^{-2} before changing to the next discharge current density of 3 mA cm^{-2}, 6 mA cm^{-2}, 8 mA cm^{-2} and 10 mA cm^{-2} discharge currents between 3 and 4.3 V. After cycling at 6, 8 and 10 mA cm^{-2}, one additional cycle was performed at 1 mA cm^{-2} respectively, to check the capacity retention. The charge current density was constantly 1 mA cm^{-2} with a consecutive constant voltage step at 4.3 V, to ensure complete delithiation of the cathode. Moreover, OCV measurements were performed in order to calculate the diffusion constant during charge and discharge respectively. This was achieved by galvanostatic titration in 1 and 5% SOC-steps at different C-Rates between C/10 and 1 C, followed by 15 and 30 min relaxation. The symmetrical coin cells used for EIS were prepared analogous to the half-cells, except for the fact, that instead of a lithium foil, a larger disc (2,011 cm^2) of the same electrode was used to face the electrode under investigation. The different electrode diameters were used in order to ensure complete overlapping of the electrode under investigation.

Measurements of conductivity, density and viscosity.— For all prepared electrolyte concentrations used in this study ionic conductivity at different temperatures was measured using a Microcell from HC-rhd instruments, which consists of a 4 platinum electrode setup and determines the conductivity by EIS. Viscosity and density measurements were performed with an Anton Paar-SVM 3000 viscometer at temperatures ranging between 10-80 °C.

Simulation Section

Simulation framework. — All simulations presented in this work have been performed with the Battery and Electrochemistry Simulation Tool BEST developed in a cooperation between Fraunhofer ITWM Kaiserslautern and DLR Institute of Engineering Thermodynamics. The model is based on our previous work[11,17] on Li-ion batteries and an extended model for transport in the electrolyte has been developed to improve simulation predictions. A summary of model equations is given in the supporting information.

Electrode structures. — Electrochemical simulations are performed on realistic virtual microstructures[34] which are developed based on tomography data . In addition to the active material realizations of anode and cathode materials do also include conductive additive and binder. Cathode microstructures have already been presented in our previous study[11] and are used here without further modifications. Graphite anodes for full cell simulations have an active material content of 61.4 vol-% resulting in a theoretical areal capacity of 9 mAh cm^{-2}. Additional information on the simulation domain is given in the supporting information.

Model parametrization. — All model parameters, including transport and thermodynamic parameters of the electrolyte and active materials, as well as kinetic parameters for lithium intercalation, are determined by model experiments or from the corresponding literature. The parametrization strategy and resulting parameters are presented in the supporting information.

Acknowledgements

The presented work was financially supported by the German ministry BMBF under the reference number 03XP0073C/D within the framework of the program "Vom Material zur Innovation". The authors want to thank Rares Scurtu (ZSW Ulm) for the measurement of the EIS. Computational support was provided, by the bwHPC initiative and the bwHPC-C5 project through associated compute services of the JUSTUS HPC facility at the University of Ulm. Furthermore, this work contributes to the research performed at CELEST (Center for Electrochemical Energy Storage Ulm-Karlsruhe). All responsibility for the content of this publication is assumed by the authors.

Keywords: High-energy Li-ion battery • concentrated electrolyte • Li-ion concentration gradient • ultra-thick NCM 622 electrode • 3D-microstructure modelling and simulation

[1] M. Marinaro, D. Bresser, E. Beyer, P. Faguy, K. Hosoi, H. Li, J. Sakovica, K. Amine, M. Wohlfahrt-Mehrens, S. Passerini, *Journal of Power Sources* **2020**, *459*, 228073.
[2] G. E. Blomgren, *Journal of The Electrochemical Society* **2017**, *164*, A5019–A5025.
[3] J. B. Goodenough, K.-S. Park, *J. Am. Chem. Soc.* **2013**, *135*, 1167–1176.
[4] W. Li, B. Song, A. Manthiram, *Chem. Soc. Rev.* **2017**, *46*, 3006–3059.
[5] Y. Yamada, A. Yamada, *Journal of The Electrochemical Society* **2015**, *162*, A2406–A2423.
[6] Y. Yamada, J. Wang, S. Ko, E. Watanabe, A. Yamada, *Nature Energy* **2019**, *4*, 269–280.
[7] Y. Yamada, *BCSJ* **2019**, *93*, 109–118.
[8] Z. Du, D. L. Wood, C. Daniel, S. Kalnaus, J. Li, *Journal of Applied Electrochemistry* **2017**, *47*, 405–415.
[9] V. Srinivasan, J. Newman, *Journal of The Electrochemical Society* **2004**, *151*, A1517–A1529.
[10] S. Hein, T. Danner, D. Westhoff, B. Prifling, R. Scurtu, L. Kremer, A. Hoffmann, A. Hilger, M. Osenberg, I. Manke, et al., *Journal of The Electrochemical Society* **2020**, *167*, 013546.
[11] L. S. Kremer, A. Hoffmann, T. Danner, S. Hein, B. Prifling, D. Westhoff, C. Dreer, A. Latz, V. Schmidt, M. Wohlfahrt-Mehrens, *Energy Technology* **2020**, *8*, 1900167.
[12] T. Danner, M. Singh, S. Hein, J. Kaiser, H. Hahn, A. Latz, *Journal of Power Sources* **2016**, *334*, 191–201.
[13] H. Zheng, J. Li, X. Song, G. Liu, V. S. Battaglia, *Electrochimica Acta* **2012**, *71*, 258–265.
[14] D. Y. W. Yu, K. Donoue, T. Inoue, M. Fujimoto, S. Fujitani, *Journal of The Electrochemical Society* **2006**, *153*, A835–A839.
[15] K. G. Gallagher, S. E. Trask, C. Bauer, T. Woehrle, S. F. Lux, M. Tschech, P. Lamp, B. J. Polzin, S. Ha, B. Long, et al., *Journal of The Electrochemical Society* **2016**, *163*, A138–A149.
[16] B. Scrosati, J. Garche, W. Tillmetz, *Advances in Battery Technologies for Electric Vehicles*, Woodhead Publishing, **2015**.
[17] A. Latz, J. Zausch, *Journal of Power Sources* **2011**, *196*, 3296–3302.
[18] Z. Du, D. L. Wood, I. Belharouak, *Electrochemistry Communications* **2019**, *103*, 109–113.
[19] M. Ue, *Journal of The Electrochemical Society* **1994**, *141*, 3336.
[20] R. J. Blint, *Journal of The Electrochemical Society* **1995**, *142*, 696.
[21] Y. Wang, S. Nakamura, M. Ue, P. B. Balbuena, *J. Am. Chem. Soc.* **2001**, *123*, 11708–11718.
[22] S. Yanase,, T. OI, *Journal of Nuclear Science and Technology* **2002**, *39*, 1060–1064.
[23] K. Xu, *Chem. Rev.* **2004**, *104*, 4303–4418.
[24] M. Lacey, *Matt Lacey* **n.d.**
[25] M. S. Ding, K. Xu, S. S. Zhang, K. Amine, G. L. Henriksen, T. R. Jow, *Journal of The Electrochemical Society* **2001**, *148*, A1196–A1204.
[26] S. Zugmann, M. Fleischmann, M. Amereller, R. M. Gschwind, H. D. Wiemhöfer, H. J. Gores, *Electrochimica Acta* **2011**, *56*, 3926–3933.
[27] J. Self, K. D. Fong, K. A. Persson, *ACS Energy Lett.* **2019**, *4*, 2843–2849.
[28] J.-K. Park, *Principles and Applications of Lithium Secondary Batteries*, John Wiley & Sons, **2012**.
[29] D. Takamatsu, A. Yoneyama, Y. Asari, T. Hirano, *J. Am. Chem. Soc.* **2018**, *140*, 1608–1611.
[30] H. Lundgren, J. Scheers, M. Behm, G. Lindbergh, *Journal of The Electrochemical Society* **2015**, *162*, A1334–A1340.
[31] H.-B. Han, S.-S. Zhou, D.-J. Zhang, S.-W. Feng, L.-F. Li, K. Liu, W.-F. Feng, J. Nie, H. Li, X.-J. Huang, et al., *Journal of Power Sources* **2011**, *196*, 3623–3632.

[32] E. R. Logan, E. M. Tonita, K. L. Gering, J. Li, X. Ma, L. Y. Beaulieu, J. R. Dahn, *Journal of The Electrochemical Society* **2018**, *165*, A21–A30.

[33] Z. Cao, M. Hashinokuchi, T. Doi, M. Inaba, *Journal of The Electrochemical Society* **2019**, *166*, A82–A88.

[34] D. Westhoff, I. Manke, V. Schmidt, *Computational Materials Science* **2018**, *151*, 53–64.

Entry for the Table of Contents

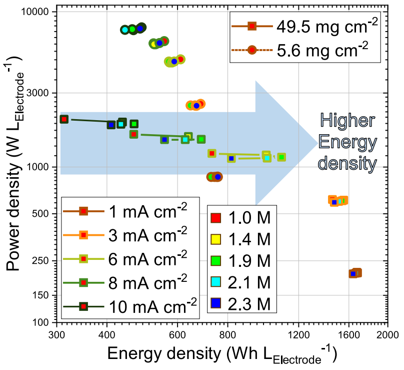

Ultra-thick electrodes offer a larger areal capacity and higher active to passive material ratio than state of the art Li-ion battery electrodes. However, they suffer from low rate capabilities, due to mass transport limitations in the electrolyte. Concentrated electrolytes above 1 mol L^{-1} increase the density of charge carriers, which mitigates Li-ion depletion and improves the energy density of ultra-thick electrodes at high current densities.

Supporting Information

Experimental Section

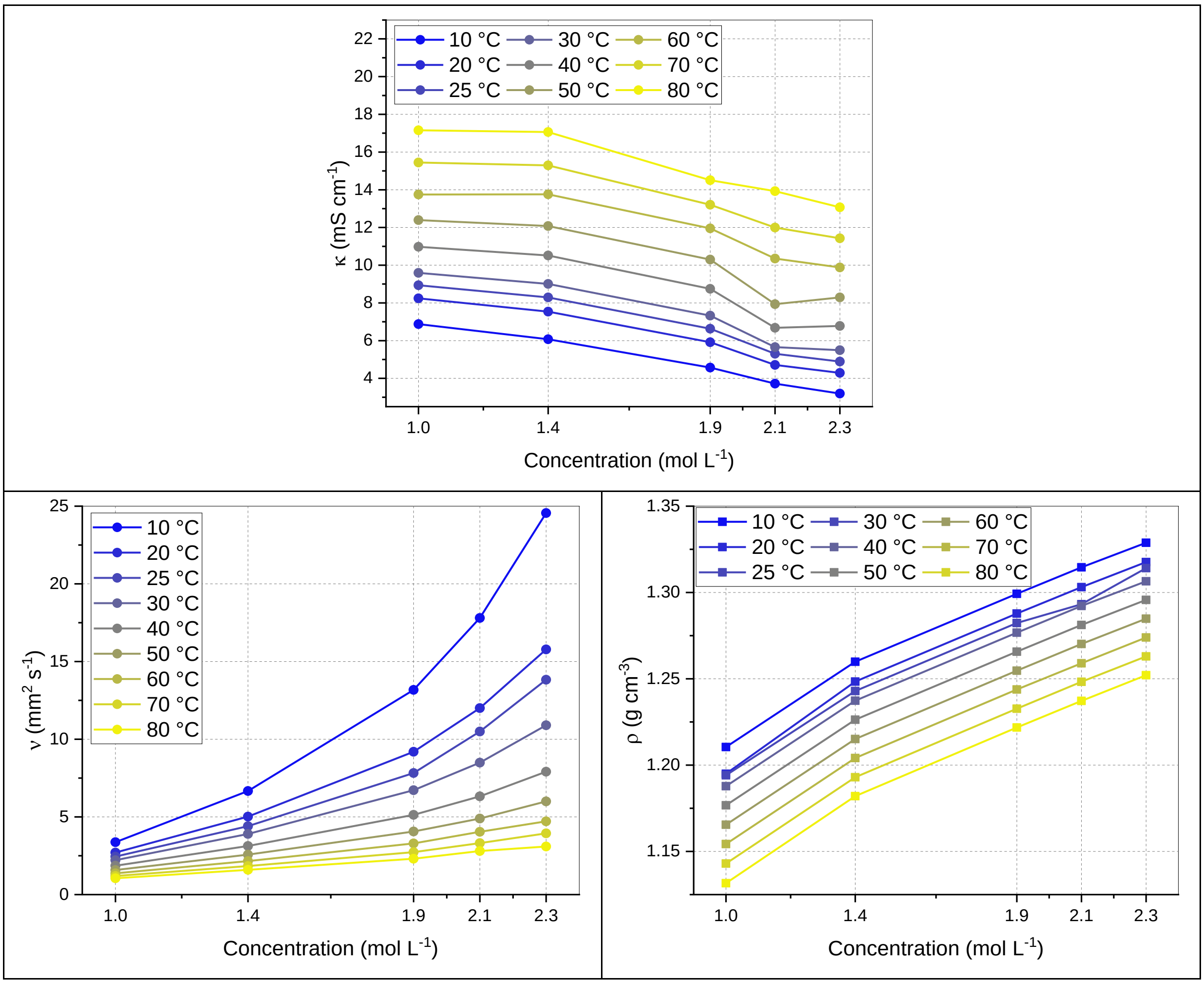

Figure S 1 Electrolyte salt concentration dependence of the electrolytic conductivity (top), kinematic viscosity (bottom left) and density at temperatures between 10 and 80 °C.

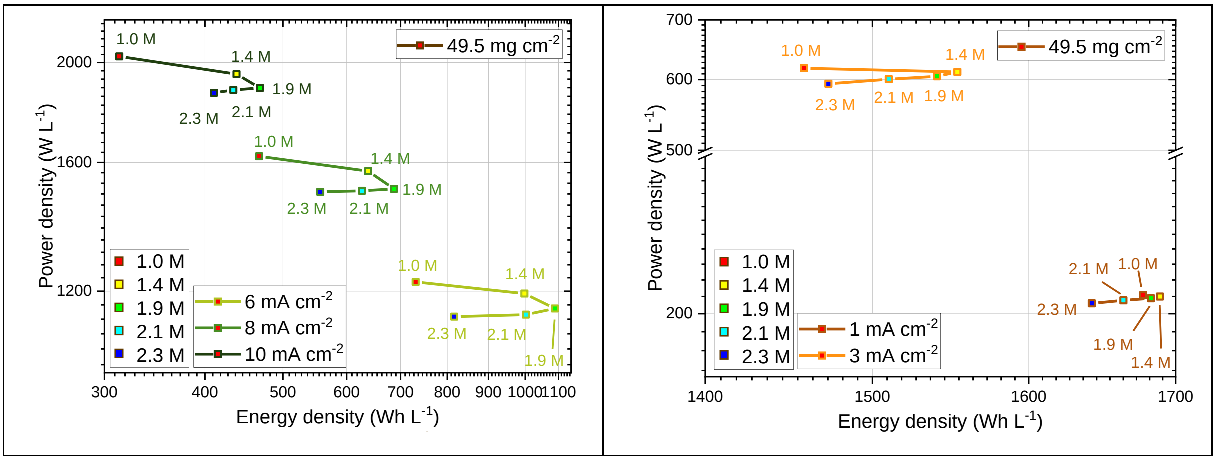

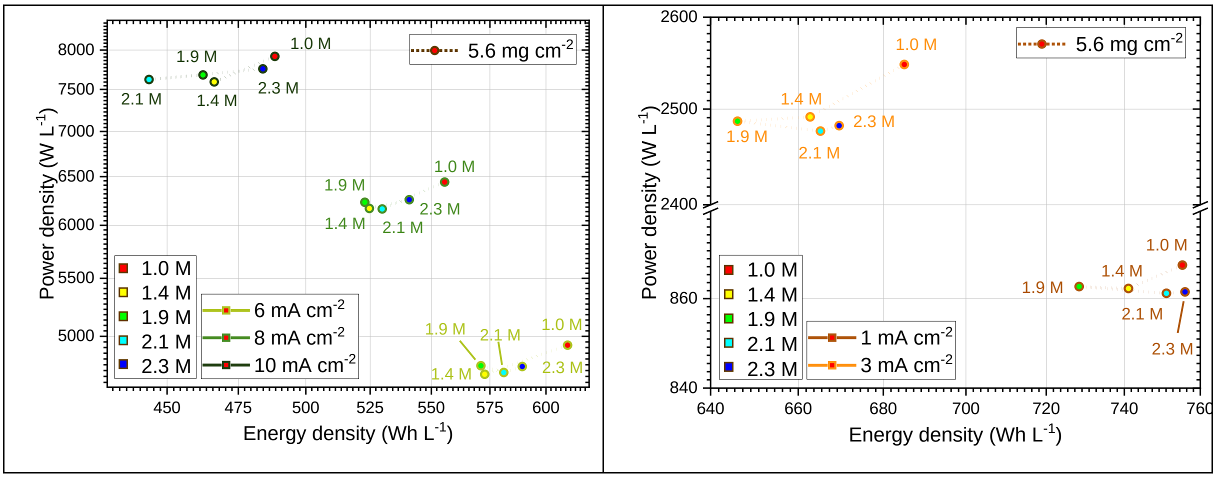

Figure S 2 Magnification of different areas in the Ragone plot from Figure 6. Top: Magnification towards higher energy densities (ultra-thick electrode) and bottom: magnification towards higher power densities (thin electrode).

Simulation Section

Details of the electrochemical model

In our previous work[1], only the impact of the CBD on the lithium transport in the electrolyte is included. In this work, the transport model, as given in [2], is further extended to also include the electronic contribution of the CBD phase. Thus, the impact of the CBD network on the electrochemical performance is fully included. The governing equations of the extended transport model are listed in Table SI 1.

The transport in the regions of the nano-porous CBD is modeled through a homogenized approach, where the mixed phase of electrolyte and CBD is described as a porous, homogeneous medium. The electronic transport in the CBD is described by Ohms law similar to the active material:

$$\vec{j}_{CBD} = -\sigma_{CBD}\vec{\nabla}\Phi_{CBD} \qquad \text{(SI-1)}$$

The lithium and charge transport in the electrolyte and the charge transport in the CBD within the CBD-region is described via an effective transport, where the transport coefficients X are modified by the respective volume fraction ϵ and the tortuosity τ as follows

$$X_{eff} = \frac{\epsilon}{\tau} X_{bulk} \qquad \text{(SI-2)}$$

The used porosity and tortuosity for the CBD-region are listed in Table SI 2.

The active surface between the electrolyte and the active material in the CBD-region is reduced by the porosity of the electrolyte. The current flowing from the active material through the interface between the CBD-region and the active material can split into the CBD and the electrolyte:

$$\begin{gathered}
\vec{j}_{So} \cdot \vec{n} = j_{CBD} + j_{intercalation} \cdot \epsilon_{El} \\
\vec{N}_{So} \cdot \vec{n} = N_{intercalation} \cdot \epsilon_{El} \\
\vec{j}_{El} \cdot \vec{n} = j_{intercalation} \cdot \epsilon_{El} \\
\vec{N}_{El} \cdot \vec{n} = N_{intercalation} \cdot \epsilon_{El} \\
\vec{j}_{CBD} \cdot \vec{n} = j_{CBD} = -\sigma_{eff,CBD}\vec{\nabla}\Phi
\end{gathered} \qquad \text{(SI-3)}$$

The intercalation reaction in Graphite is described via a classical Butler-Volmer-expression

$$i_{intercalation} = 2 \cdot i_{00}^{intercalation} \cdot \sqrt{c_{El}} \cdot \sqrt{c_{So}} \sqrt{c_{So}^{max} - c_{So}} \cdot sinh\left(\frac{F}{2RT} \eta_{intercalation}\right) \tag{SI-4}$$

with the exchange current density $i_{00}^{intercalation}$ and the overpotential η driving the reaction. The intercalation in NCM is described with the expression derived in [3].

$$i_{intercalation} = 2 \cdot i_{00}^{intercalation} \cdot \sqrt{c_{El}} \cdot \sqrt{c_{So}} \cdot sinh\left(\frac{F}{2RT} \eta_{intercalation}\right) \tag{SI-5}$$

In both cases the overpotential is given by

$$\eta_{intercalation} = \Phi_{So} - \varphi_{El} - U_0(c_{So}) \tag{SI-6}$$

Table S 1. The constitutive equations of the Li-ion battery model used in this work. Indices are defined as Electrolyte= El, Active material= So and Carbon additive = CB.

Phase	Material balance	Charge balance
Electrolyte	$\frac{\partial c_{\mathrm{El}}}{\partial t} = -\vec{\nabla} \cdot \vec{N}_{\mathrm{eff,El}}$	$0 = -\vec{\nabla} \cdot \vec{j}_{\mathrm{eff,El}}$
Active material	$\frac{\partial c_{\mathrm{So}}}{\partial t} = -\vec{\nabla} \cdot \vec{N}_{\mathrm{So}}$	$0 = -\vec{\nabla} \cdot \vec{j}_{\mathrm{So}}$
Carbon additive	-	$0 = -\vec{\nabla} \cdot \vec{j}_{\mathrm{eff,CB}}$
Phase	Lithium flux	Charge flux
Electrolyte	$\vec{N}_{\mathrm{eff,El}} = -\mathrm{D}_{\mathrm{eff,El}} \vec{\nabla} c_{\mathrm{El}} + \vec{j}_{\mathrm{eff,El}}$	$\vec{j}_{\mathrm{eff,El}} = -\sigma_{\mathrm{eff}} \vec{\nabla} \varphi_{\mathrm{El}}$
Carbon additive	-	$\vec{j}_{\mathrm{eff,CB}} = -\kappa_{\mathrm{eff,CB}} \vec{\nabla} \Phi_{\mathrm{So}}$
Active material	$\vec{N}_{\mathrm{So}} = -D_{\mathrm{So}} \vec{\nabla} c_{\mathrm{So}}$	$\vec{j}_{\mathrm{So}} = -\kappa_{\mathrm{So}} \vec{\nabla} \Phi_{\mathrm{So}}$

U_0^{Gr} (soc) = 0.6379 + 0.5416*exp(-305.5309*soc) + 0.044*tanh(-(soc-0.1958)/0.1088) - 0.1978*tanh((soc-1:0571)/0.0854) - 0.6875*tanh((soc+0.0117)/0.0529) - 0.0175*tanh((soc-0.5692)/0.0875) *(SI-7)*

$$\kappa_{NMC} = exp(-202.91 * soc^4 + 322.38 * soc^3 - 178.24 * soc^2 + 50.07 * soc - 13.47) \tag{SI-8}$$

Table SI-2 List of the electrochemical parameters used for the simulations.

Parameter	Value	Description
NCM		
c_{NCM}^0 / mol/cm^3	1.6500e-2	Initial Li concentration
c_{NCM}^{max} / mol/cm^3	5.0451e-2	Maximum Li concentration

D_{NCM} / cm^2/s	See Figure S 4	Li-ion diffusion coefficient
κ_{NCM} / S/cm	See *(SI-7)*	Electronic conductivity of NCM
U_0 / V	See Figure S 4	Open circuit potential of NCM
Graphite		
c_{Gr}^{0} / mol/cm^3	2.4295e-2	Initial Li concentration
c_{Gr}^{max} / mol/cm^3	3.0369e-2	Maximum Li concentration
D_{Gr} / cm^2/s	3.9e-10	Li-ion diffusion coefficient
κ_{Gr} / S/cm	1	Electronic conductivity of Graphite
U_0^{Gr} / V	See *(SI-6)*	Open circuit potential of Graphite
Electrolyte		
c_{El}^{0} / mol/l	1	Concentration of Li salt
κ_{El} / S/cm	See Figure S 3	Conductivity
D_{El} / cm^2/s	See Figure S 3	Li-ion diffusion coefficient
f_{Li}^{Elyte} / -	See Figure S 3	Activity factor
$t_{\pm}$ / -	See Figure S 3	Transference number
κ_{CC} / S/cm	100	Electronic conductivity of Current collector (estimated)
κ_{CC} / S/cm	10	Electronic conductivity of carbon in passive material phase (estimated)
Kinetic parameter		
i_{00}^{Li} / A/cm^2	0.06407	Exchange current density factor at lithium electrode
i_{00}^{Gr} / Acm$^{2.5}$/mol$^{1.5}$	0.367	Exchange current density factor for intercalation
i_{00}^{NMC} / A cm/mol	0.23047	Exchange current density factor for intercalation

Model Parametrization

All model parameters, including transport and thermodynamic parameters of the electrolyte and active materials, as well as kinetic parameters for lithium intercalation, are determined by model experiments or from the corresponding literature. Note, that all parameters are determined independently in order to improve qualitative model predictions.

Electrolyte – Electrolyte parameters are key to understand the results in this study. Several groups report transport parameters for the solvent and salt system[4,5] Additionally, we performed our own measurements to complement the information presented in the literature. However, in none of the studies measurements of all parameters are done up to the solubility limit. An overview of data points and the corresponding correlations at room temperature (25 °C) which are used in our simulations are shown in Figure S 3. In order to do the simulations, the correlations extrapolate transport properties well beyond the solubility limit. While some supersaturation of the electrolyte is possible, especially during operation of the cell, deviations of transport properties from the correlations are expected.

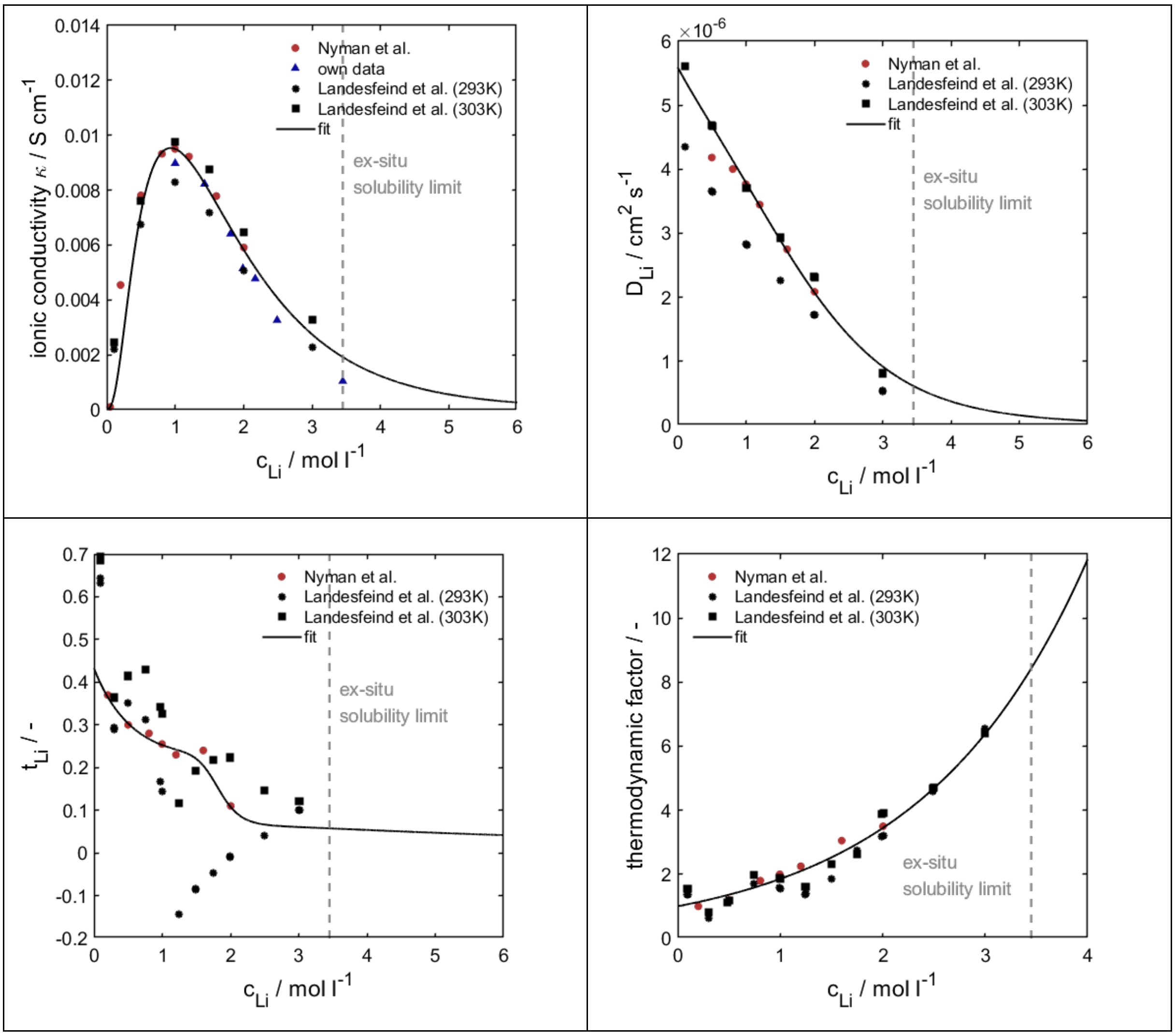

Figure S 3 – Overview of electrolyte parameters compiled from different sources in the literature and our own experiments. Solid lines indicate correlations used in this study.

Active material – In this study we focus on ultra-thick electrodes consisting of NCM 622 active material. GITT measurements on thin electrodes were performed to extract open circuit voltage and the lithium chemical-diffusion coefficient as function of lithium stoichiometry. Details of the approached are also outlined in [6]. Additionally, we perform at each state of charge current pulses with different magnitude in order to determine kinetic parameters. In our simulations, however, we use a mean value over the whole soc range. The corresponding results are presented in Figure S 4.

Parameters of the lithium metal electrode and the graphite material which is used in full cell simulations are taken from different sources in the literature[7–9]. A detailed determination of model parameters as it was done for the NCM 622 electrodes is not in the focus of this work.

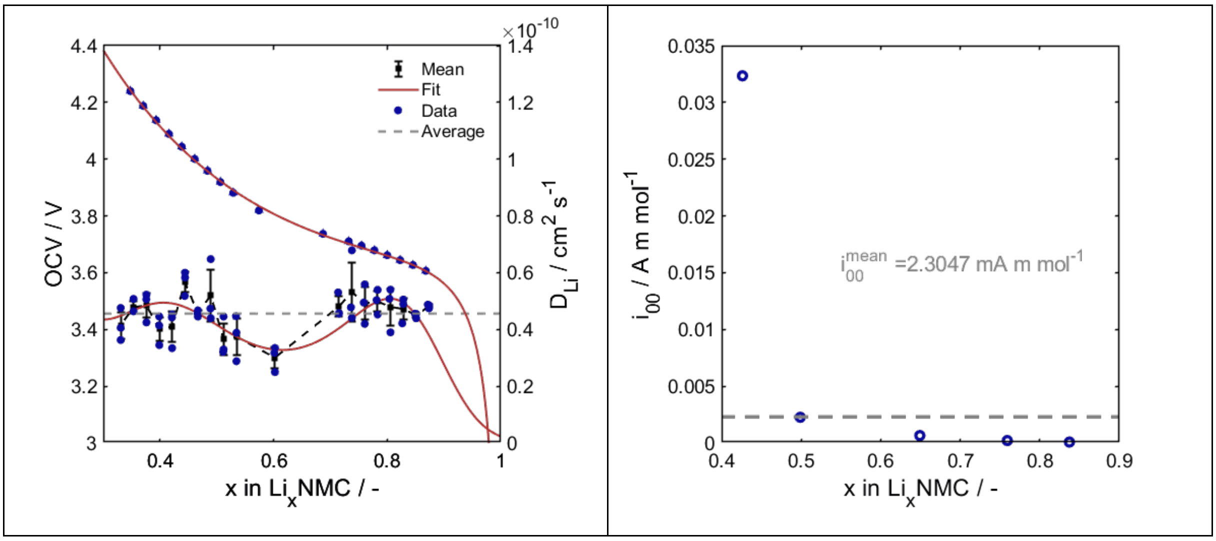

Figure S 4 – Open circuit voltage, chemical diffusion coefficient (left) and exchange current density of the intercalation reaction (right) as function of lithium content. Parameters are determined by GITT measurements on thin model electrodes.

Electrode tortuosity – Simulations in this work are done on realistic virtual microstructures including passive materials, i.e. carbon black and binder, as a homogenized phase. Both pore networks, between the active material particles and within the homogenized passive material phase, contribute to the electrode tortuosity. Previously, we demonstrated that the information provided by impedance measurements on symmetrical cells can be used to extract the tortuosity factors of the porous passive material phase which is hard to resolve using non-destructive imaging techniques[1]. Details of the approach can be found in our previous publication. Figure S 5 presents measurements and simulations of symmetrical cells consisting of ultra-thick NCM 622 electrodes. The tortuosity of the passive material phase was adjusted in the simulations in order to reproduce the experimental data i) in the high frequency range (red line) and ii) low frequency limit (black line). The resulting effective conductivity of the passive material phase is 0.12 and 0.07, respectively. Both values are slightly larger than anticipated in our previous simulations on the same structures where the detailed characterization of the electrode material was not yet available [9].It is interesting to notice that in both cases the simulations reproduce two features at high frequencies which are also present in the experiments. The origin of such features is typically attributed to contact resistances at the current collector. Additional studies investigating these effects are work in progress.

In the graphite anode we assume the same effective transport parameters and porosity like in the NCM 622 electrode.

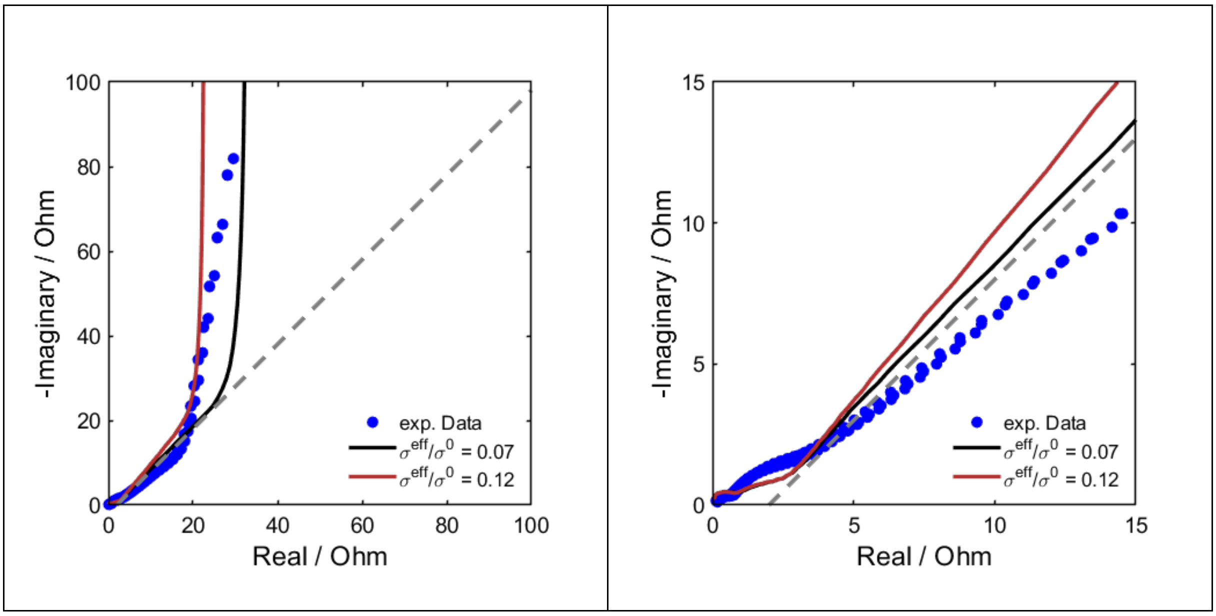

Figure S 5 – Impedance measurements and simulations on symmetrical cells. Values are corrected by the high frequency resistance. Left: Overview over whole frequency range. Right: Zoom to high frequencies.

Electrode structures and simulation domain.

Realizations of electrode structures are produced with stochastic microstructure generators developed at the Institute of Stochastics, Ulm University. Details of the approach are given in [10]. Realizations of cathode microstructures have been presented and analysed in our previous study on the manufacturing process of ultra-thick cathodes[9]. NCM 622 structures refer to the case labeled as 'low shear mixing'. The anode used for full-cell simulations has been modelled by the excursion set of a Gaussian random field [11]. For this purpose, the volume fraction of active material of 61.4% has been computed from the material composition of an experimentally manufactured graphite anode. The 3D morphology of this anode has been measured by synchrotron tomography and subsequently binarized by a global threshold such that the volume fraction of 61.4% is matched. The binarized image data allows for computing the two-point coverage probability function using the Fourier-based approach described in [12]. Afterwards, the two-point coverage probability function is converted to the covariance function of the Gaussian random field using Equation 6.158 from [13]. Finally, the Gaussian random field is simulated by means of the approach described in [14]. The ultra-thick virtual graphite anode was adjusted in thickness in order to provide a theoretical capacity of 9 mAh cm^{-2}. Passive materials have been distributed homogeneously at contact points to the active material as described in [Hein 2020]. In both electrodes we assume a porosity of the passive material phase of 50%. An overview of structural parameters and electrode composition is provided in Table S 1. The electrodes are assembled to virtual half-cells, full-cells, and symmetric cells. In all cases we model a glass fiber separator between the electrodes. The thickness of the separator is assumed to be 100 µm due to compression in the coin cells. The resulting porosity of the separator is assumed to be 50% with a tortuosity of the pore space approaching 1. The x-direction in our simulation represents the normal vector pointing from anode to cathode.

Table S 1 – Structural parameters and composition of electrodes

Sample	**NCM 622**	**Graphite**
Dimensions (*x*,y,z voxels)	187, 125, 125	208, 125, 125
Resolution / µm	0.876	0.876
Composition / vol-%		
AM	56.9	61.4

Electrolyte	19.1	27.1
Passive Materials	24.0	11.5

Simulation results

Model validation on half-cells – Figure S 6 presents discharge curves of ultra-thick NCM 622 cathodes for varying initial salt concentration. Experiments are given by solid symbols and lines represent simulation data. Simulations are performed for the two effective conductivities in the passive material as extracted from the symmetrical cells. The shaded areas between the curves represents the range of simulation results within this parameter range. In all cases the simulations are in fair agreement with the experimental data. At 1M and 1.4M initial salt concentration the capacity of the samples is well represented by the simulations with lower passive material effective electrolyte conductivity. At higher concentrations better agreement for the other limiting case can be reported. In general, we observe strong deviations between simulations and experiments at high salt concentrations and currents. The spatial distribution at the end of the discharge indicates that concentration gradients are significant and local maxima are well beyond the solubility limit, which we found in experiments (cf. Figure S 7). This indicates that the speciation in the electrolyte has a significant effect on transport phenomena. Moreover, precipitation of the electrolyte salt can be expected. Both effects are not covered in our model. This highlights the need for improved transport models for highly concentrated electrolytes which are to our knowledge not presented in the literature.

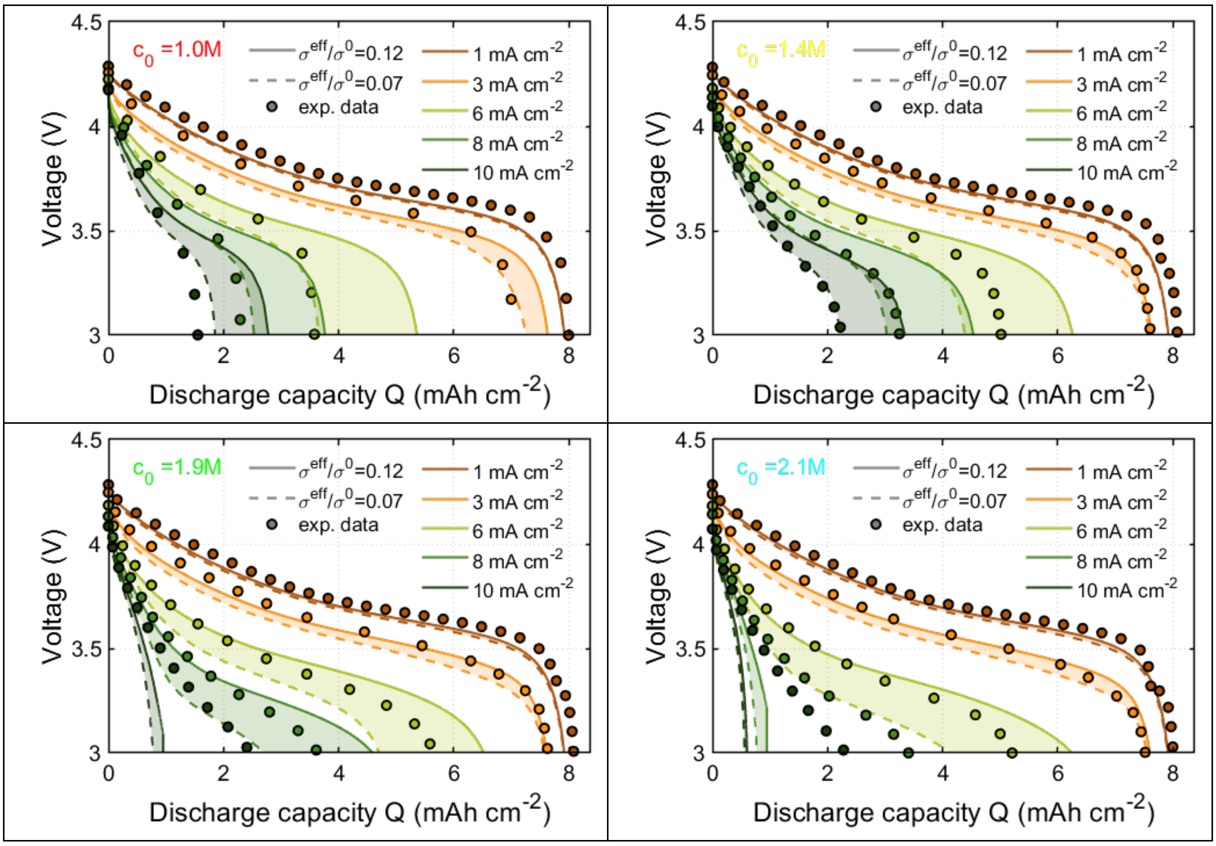

Figure S 6 – Discharge curves of ultra-thick NCM 622 cathodes in half-cell configuration for different initial salt concentration c_0. Experiments are given by solid symbols and simulations by corresponding lines. Shaded areas represent the parameter space given by the two values for effective conductivity extracted from symmetrical cells.

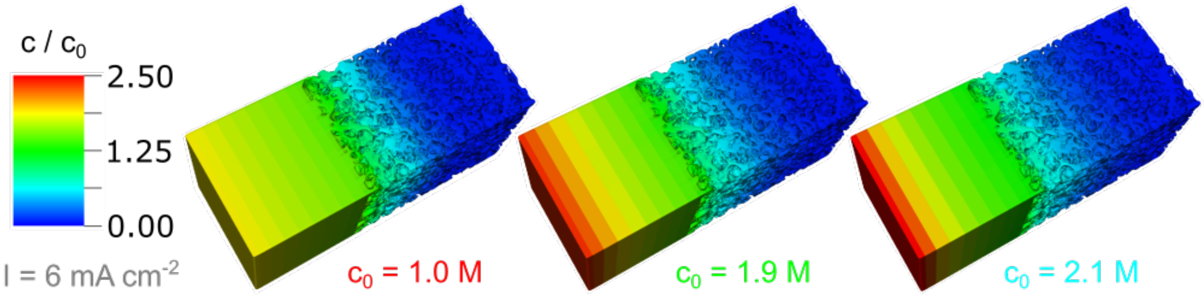

Figure S 7 – Normalized concentration distribution in electrolyte at the cut-off voltage of 3.0V for increasing initial salt concentration (left to right). The applied discharge current in the half-cell simulations is in all cases 6 mA cm^{-2}. The effective conductivity of the passive materials is 0.12.

Full cell simulations – Figure S 8 presents simulation results of full-cells consisting of ultra-thick NCM cathodes and graphite anodes. The data is the basis for the calculation of relative energy densities in Figure 8 of the main article. Corresponding normalized concentration distributions are also presented in Figure S 9. The simulations indicate that extremely high concentration gradients can be expected.

An overview of the simulated capacity retention is shown in Figure S 10. Note, that predicted capacity gain in full-cell configuration is larger than in half-cells at the same concentration and current.

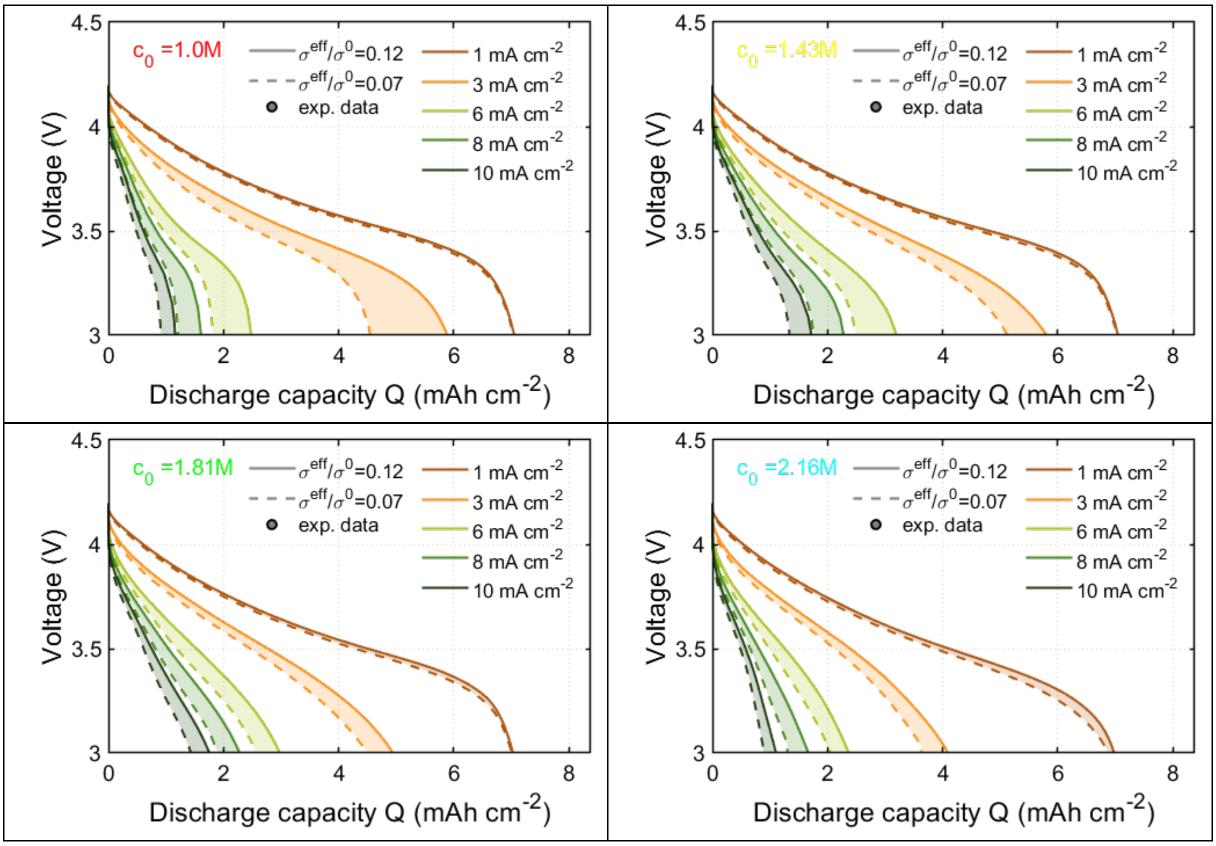

Figure S 8 – Simulated discharge curves of ultra-thick NCM 622 graphite full-cells with varying initial salt concentration.

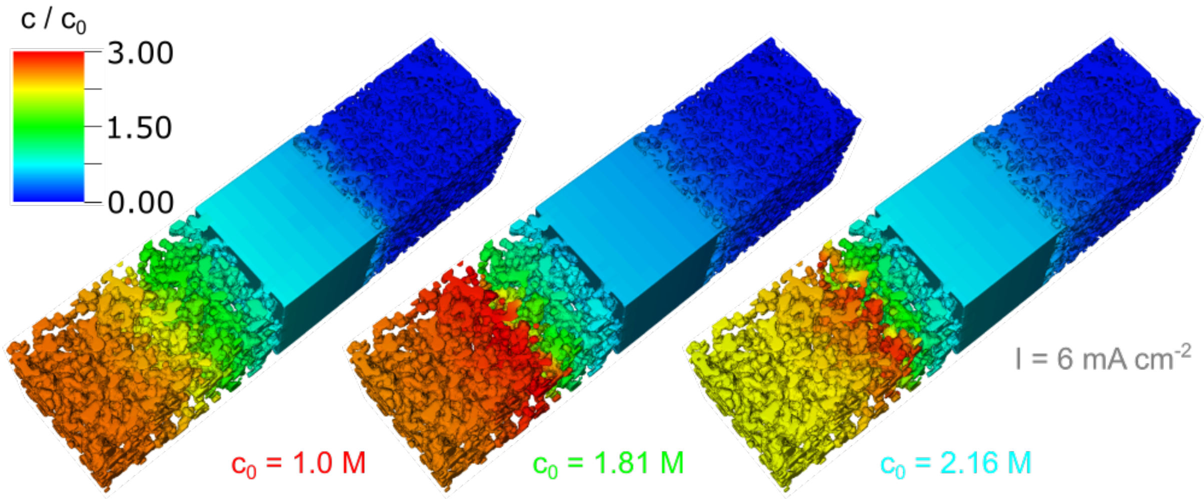

Figure S 9 - Normalized concentration distribution in electrolyte at the cut-off voltage of 3.0V for increasing initial salt concentration (left to right). The applied discharge current in the full-cell simulations is in all cases 6 mA cm^{-2}. The effective conductivity of the passive materials is 0.12.

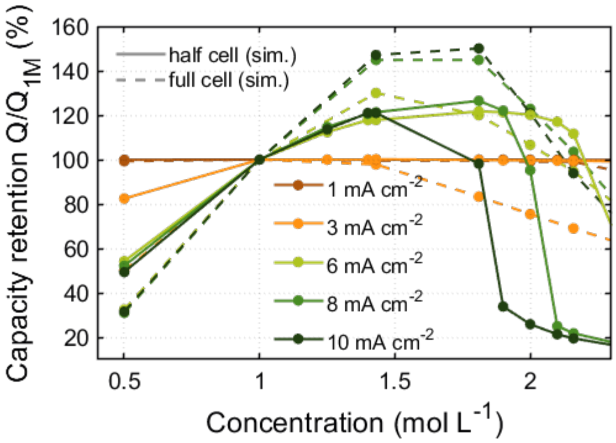

Figure S 10 – Simulated discharge capacity normalized by the capacity for an initial salt concentration of 1 M. Solid lines represent half-cell simulations. Dashed lines are obtained from full-cell simulations. The effective conductivity of the passive materials is 0.12.

References

[1] S. Hein, T. Danner, D. Westhoff, B. Prifling, R. Scurtu, L. Kremer, A. Hoffmann, A. Hilger, M. Osenberg, I. Manke, M. Wohlfahrt-Mehrens, V. Schmidt, A. Latz, *J. Electrochem. Soc.* **2020**, *167*, 013546.
[2] A. Latz, J. Zausch, *J. Power Sources* **2011**, *196*, 3296–3302.
[3] A. Latz, J. Zausch, *Electrochem. Adv. Mater. Technol. Instrum.* **2013**, *110*, 358–362.
[4] A. Nyman, M. Behm, G. Lindbergh, *Electrochimica Acta* **2008**, *53*, 6356–6365.
[5] J. Landesfeind, H. A. Gasteiger, *J. Electrochem. Soc.* **2019**, *166*, A3079–A3097.
[6] D. Westhoff, T. Danner, S. Hein, R. Scurtu, L. Kremer, A. Hoffmann, A. Hilger, I. Manke, M. Wohlfahrt-Mehrens, A. Latz, V. Schmidt, *Mater. Charact.* **2019**, *151*, 166–174.
[7] M. Safari, C. Delacourt, *J. Electrochem. Soc.* **2011**, *158*, A562.
[8] S. Hein, Modeling of Lithium Plating in Lithium-Ion-Batteries, Ulm University, **2018**.
[9] L. S. Kremer, A. Hoffmann, T. Danner, S. Hein, B. Prifling, D. Westhoff, C. Dreer, A. Latz, V. Schmidt, M. Wohlfahrt-Mehrens, *Energy Technol.* **2020**, *8*, 1900167.
[10] D. Westhoff, I. Manke, V. Schmidt, *Comput. Mater. Sci.* **2018**, *151*, 53–64.

[11] C. Lantuéjoul, *Geostatistical Simulation: Models and Algorithms*, Springer Science & Business Media, **2013**.
[12] J. Ohser, K. Schladitz, *3D Images of Materials Structures: Processing and Analysis*, John Wiley & Sons, **2009**.
[13] S. N. Chiu, D. Stoyan, W. S. Kendall, J. Mecke, *Stochastic Geometry and Its Applications*, John Wiley & Sons, **2013**.
[14] A. Lang, J. Potthoff, *Monte Carlo Methods Appl.* **2011**, *17*, 195–214.